Constraints for flow regimes on smooth fracture surfaces

Teamrat A. Ghezzehei

Earth Sciences Division, Lawrence Berkeley National Laboratory, Berkeley, California, USA

Received 4 March 2004; revised 4 May 2004; accepted 21 June 2004; published 4 November 2004.

[1] In recent years, significant advances have been made in our understanding of the complex flow processes in individual fractures, aided by flow visualization experiments and conceptual modeling efforts. These advances have led to the recognition of several flow regimes in unsaturated individual fractures subjected to different initial and boundary conditions. For an idealized smooth fracture surface the most important regimes are film flow, rivulet flow, and sliding of droplets. The existence of such significantly dissimilar flow regimes has been a major hindrance in the development of self-consistent conceptual models of flow for single fracture surfaces that encompass all the flow regimes. The objective of this study is to delineate the existence of the different flow regimes in individual fracture surfaces. For steady state flow conditions, we developed physical constraints on the different flow regimes that satisfy minimum energy configurations, which enabled us to segregate the wide range of fracture flux (volumetric flow rate per fracture width) into several flow regimes. These are, in increasing order of flow rate, flow of adsorbed films, flow of sliding drops, rivulet flow, stable film flow, and unstable (turbulent) film flow. The scope of this study is limited to wide-aperture smooth fractures with the flow on the opposing sides of fracture being independent. *INDEX TERMS:* 1829 Hydrology: Groundwater hydrology; 1875 Hydrology: Unsaturated zone; 1899 Hydrology: General or miscellaneous; *KEYWORDS:* constraints, drop, film, fracture, rivulet, unsaturated

Citation: Ghezzehei, T. A. (2004), Constraints for flow regimes on smooth fracture surfaces, *Water Resour. Res.*, *40*, W11503, doi:10.1029/2004WR003164.

1. Introduction

[2] The development of realistic and robust predictive models of flow and transport in fractured geologic media requires a thorough understanding of the physical processes that govern flow in individual fractures. In recent years, significant advances have been made in our knowledge of these complex processes, aided by flow visualization experiments and conceptual modeling of single-fracture flows [e.g., *Amundsen et al.*, 1999; *Bertels et al.*, 2001; *Detwiler et al.*, 2002; *Dobson et al.*, 2003; *Doe*, 2001; *Dragila*, 1999; *Fourar et al.*, 1993; *Glass and Nicholl*, 1996; *Glass et al.*, 2002; *Kneafsey and Pruess*, 1998; *Nicholl et al.*, 1994; *Or and Tuller*, 2000; *Persoff and Pruess*, 1995; *Su et al.*, 1999, 2001; *Tokunaga and Wan*, 1997; *Tokunaga et al.*, 2000; *Zhong et al.*, 2001]. One important outcome of these endeavors is the recognition that several flow regimes exist in individual fractures that are subjected to different initial and boundary conditions.

[3] The simplest flow regime, both physically and mathematically, involves a stable and flat film of liquid that lines the entire surface of planar and smooth fractures. Using laboratory flow experiments, *Tokunaga and Wan* [1997] demonstrated that film flow is a very important mechanism of flow in unsaturated fractured media. Their findings were followed by a surge of interest in the role of films in vadose zone processes [e.g., *Amundsen et al.*, 1999; *Berkowitz*, 2002; *Bertels et al.*, 2001; *Kneafsey and Pruess*, 1998; *Or and Tuller*, 2000; *Pruess*, 1999; *Tokunaga and Wan*, 2001; *Tokunaga et al.*, 2000]. Such flat films are inherently unstable. At high-flow rates, capillary forces and/or inertia create waves (ripples) that travel on the film surface [*Berbente and Ruckenst*, 1968; *Brauner*, 1989; *Jayanti and Hewitt*, 1997; *Lee*, 1969; *Patnaik and Perez-Blanco*, 1996; *Penev et al.*, 1972; *Soo*, 1996; *Yih*, 1963]. These surface waves can be responsible for enhanced travel velocity and transport in unsaturated fractures, which cannot be explained by stable film flow alone [*Dragila*, 1999; *Dragila and Wheatcraft*, 2001]. On the other hand, at lower-flow rates, the films disintegrate into thin threads or rivulets [*Bankoff*, 1983; *El-Genk and Saber*, 2001; *Hughes and Bott*, 1998; *Joo et al.*, 1996]. Similar formation of rivulets in narrow-aperture fractures was observed by *Su et al.* [1999, 2001]. At even lower-flow rates, the threads and rivulets break up into trains of sliding drops [*Schmuki and Laso*, 1990] and blobs [*Su et al.*, 1999, 2001]. *Doe* [2001] contends that these sliding drops could play an important role in the unstable flow phenomena observed in fractured media. At extremely low-flow rates, flow in fractures is carried by thin adsorbed films, on the order of a few molecular layers [*Or and Tuller*, 2000; *Tuller et al.*, 1999].

[4] The existence of such significantly dissimilar flow regimes poses a major challenge in the pursuit of a unified, self-consistent conceptual model of flow for a single fracture and a network of fractures. The problem is apparent in most numerical simulators, which lack adequate and unified representation of the various flow regimes. In fact, the Committee on Fracture Characterization and Fluid Flow of the *National Academy of Sciences* [1996] concluded that

Table 1. Contact Angles of Smooth Surfaces[a]

Substrate	Water Contact Angle, deg
Untreated glass[b]	32 ± 2
Water-rinsed glass[b]	25
Plasma-cleaned glass[b]	<10
H_2O_2-cleaned glass[b]	<10
Quartz[c]	22 ± 4

[a]See *Summer et al.* [2004].
[b]Smooth microcover glass, number 1.
[c]Quartz cover slips, substrate grade.

"most of the error involved in predicting flow behavior [in rock fractures] with a numerical model is usually due to deficiencies in the underlying conceptual models." For example, the consequences of assuming fully wetting film flow (when in fact, the flow is occurring in rivulets) could mean a gross overestimation of contaminant travel time and/or diffusion into matrix [see *Dragila and Weisbrod*, 2003, Table 1].

[5] The lack of full understanding of the constraints on the potential flow regimes, and the transitions between them, is a critical hurdle in integrating the flow regimes into a unified conceptual model. The mathematical expressions devised to model certain flow regimes (e.g., stable films, rivulets) are often used without sufficient constraints concerning the physical existence of the assumed regime. As a result, models of competing flow regimes are expected to yield vastly different results for identical boundary and initial conditions.

[6] The foregoing discussions assert the need for a common set of criteria by which all potential flow regimes can be tested and compared, thereby enabling identification of the most likely regime for a given set of flow conditions. The objective of this study was to set physical constraints for some common flow regimes, by seeking the regime that satisfies a minimum energy configuration. By focusing on the steady state pictures alone, we were able to derive analytical and semianalytical expressions for the bounds of the different flow regimes.

[7] This paper is organized as follows. In section 2, the major fracture and liquid properties that control fluid flow are summarized. Section 3 introduces the conceptual models of the various flow regimes considered in this study followed by brief review of the corresponding flow and energy equations. Section 4 compares the relative energies of the different flow regimes derived in section 3 and identifies the regime with the minimum total energy as the dominant (most likely) regime for the given flow conditions. Summary of the main findings of this study and the conclusions drawn based on them are given in the final section 5.

2. Fracture and Liquid Properties

[8] Perhaps the most challenging aspect of modeling flow in fractured media is characterization of individual fractures and fracture networks. Within a single fracture, numerous features of the fracture have strong bearing on the prevalent flow processes; these include roughness, inclination, aperture, and matedness [*Hakami and Larsson*, 1996]. A standard system of representation for these geometric features is yet to be developed. On the other hand, the physical properties of the flowing liquid are rather constant. If needed, changes in these properties due to variations in chemistry, temperature, or pressure are straightforward to account for. The single most important parameter that describes the interaction between fracture surfaces and the flowing liquid is the contact angle. In sections 2.1 and 2.2 we outline sets of simplifying assumptions regarding the fracture geometry and contact angle.

2.1. Fracture Geometry

[9] We chose a simple fracture geometry that enables us to explore flow behaviors over a wide range of flow rates. The important features of this simple geometry are the following: (1) The fracture is smooth enough with negligible effects on the liquid flow. (2) The fracture aperture (opening) is large enough for the flows along the two faces of the fracture to be considered independent. (3) The fracture surface is planar, and a single inclination angle suffices to describe the gravitational head gradient.

2.2. Intrinsic and Apparent Contact Angles

[10] The contact angle that a liquid drop at rest makes with a substrate is a manifestation of the balance between cohesive and adhesive forces. The equilibrium (intrinsic) contact angle of a liquid on clean and molecularly smooth surfaces (e.g., surface of mineral grains) is a function of the interplay between the solid-liquid, solid-vapor, and liquid-vapor interfacial energies as given by Young's equation

$$\cos\theta = \frac{\sigma_{SV} - \sigma_{SL}}{\sigma_{LV}} \tag{1}$$

where σ is the surface free energy (surface tension), and the subscripts L, S, and V denote liquid, solid, and vapor, respectively. Contact angles of water on some smooth glassy surfaces are given in Table 1.

[11] Most natural surfaces including fracture faces are neither clean nor smooth, and the solid-liquid and solid-vapor interfacial energies are not uniform throughout the surfaces. Therefore the apparent contact angle a liquid makes with a chemically and/or geometrically heterogeneous surface is deemed different from the intrinsic values. The effect of heterogeneity on contact angle is discussed in depth by *Adamson and Gast* [1997]. The apparent contact angle (θ_0) a liquid makes with a chemically homogenous surface but with geometric features that resemble a screen (or woven material) is described by Cassie's law [*Cassie*, 1948; *Packham*, 2003],

$$\cos\theta_0 = (1 - \varphi)\cos\theta - \varphi \tag{2}$$

where φ is the fraction of the surface occupied by local maxima (e.g., tips of microcrystals), which can be considered as a measure of the microroughness. In general, Cassie's law implies that the apparent contact angle is usually larger than the intrinsic value and that the enhancement of the apparent contact angle over the intrinsic value increases with openness (fewer maxima) of the microroughness. Natural evidence of this concept is apparent on the hydrophobicity of duck's back ($\theta_0 \approx 150^\circ$) because the interlocking barbules (with intrinsic contact angle of $\theta_0 \approx 100^\circ$) create microroughness with $\varphi \approx$

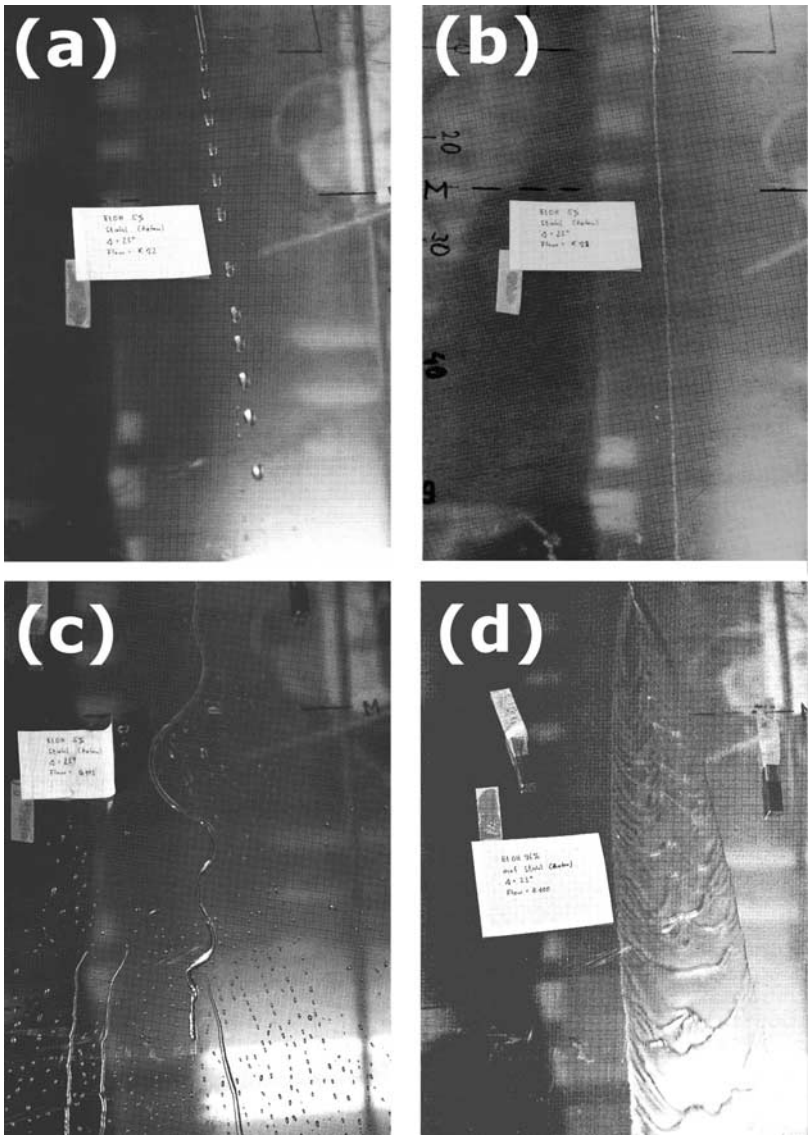

Figure 1. Photos of different flow regimes from experiments conducted by *Schmuki and Laso* [1990]: (a) sliding drops, (b) straight rivulet, (c) meandering rivulets, and (d) wavy film flow. (Reprinted with permission from Cambridge University Press.)

0.5 [*Adamson and Gast*, 1997]. Similarly, *Muller et al.* [2001] showed that the advancing contact angle of water monotonically increases from approximately 40° for flat silicone surface to approximately 55° for silicone substrate coated with germanium nanopyramids at a density of approximately 40 μm^{-2}. In general, it is believed that apparent angle is greater on rough surfaces than smooth surfaces of the same material [*Dettre and Johnson*, 1964].

[12] Without going into the details of measuring fracture surface microroughness, we assume that θ_0 is an experimentally measurable quantity. Most of the illustrative calculations shown in this paper use an apparent contact angle of $\theta_0 = 20°$ (similar to that of clean quartz as shown in Table 1). In the summary (section 5), the role of a wider range of contact angles ($0° \leq \theta_0 \leq 90°$) is shown.

3. Flow and Energy Equations

[13] The main objective of this study is to set constraints on the steady state flow rate so as to delineate the existence of various flow regimes. Transient phenomena, such as fingering of a wetting front as a liquid invades a dry fracture, are not considered. However, we do not preclude inherently unstable flow regimes (such as intermittent rivulet snapping) that occur under globally steady state flow conditions. Moreover, we are not concerned with the full detail of the transition from one regime to another that arises because of changes in boundary conditions.

[14] Photographs of flow visualization experiments conducted by *Schmuki and Laso* [1990] (shown in Figure 1) are used to explain the classification of flow regimes employed in this paper. In these experiments, liquid was delivered to the upper edge of an inclined smooth surface at a steady flow rate using narrow tubing. Figure 1 shows snapshots taken at different flow rates. At the lowest-flow rate in the experiments, *Schmuki and Laso* [1990] observed a train of equally spaced "sliding drops" (Figure 1a). When the flow rate was increased, the sliding drops began to touch and a "straight rivulet" was formed as shown in decrease in

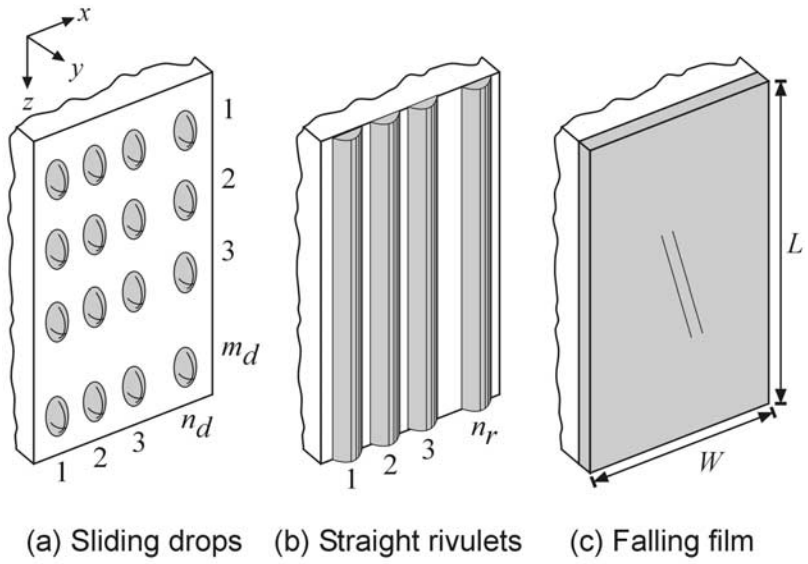

Figure 2. Conceptual geometries of flow regimes used in this study. (a) Sliding drops, (b) straight rivulets, and (c) falling film.

Figure 1b. Further increase in flow rate resulted in meandering rivulet, which bifurcated into multiple smaller rivulets (Figure 1c). At the highest-flow rate in the experiments, *Schmuki and Laso* [1990] observed a wide falling "film" with wavy surface (Figure 1d).

[15] The approach we use to discern the most stable flow regime for a given flow condition is that of "minimum energy configuration". The concept of minimum energy configuration has been used to estimate the minimum film thickness before it breaks up into rivulets [*Hobler*, 1964]. The method has been refined and used to study film and rivulet flows on flat surfaces, and inside and outside surfaces of pipes [*Bankoff*, 1971; *El-Genk and Saber*, 2001; *Mikielewicz and Moszynski*, 1976; *Ponter and Aswald*, 1977; *Schmuki and Laso*, 1990].

[16] The concept of minimum energy configuration states that the configuration with the lowest total energy (sum of kinetic and interfacial potential energies) per unit width of fracture has the highest likelihood of occurrence. Mathematically, the total system energy is given by

$$E_T = E_K + A_{SL}\sigma_{SL} + A_{SV}\sigma_{SV} + A_{LV}\sigma_{LV} \tag{3}$$

where A and σ denote interfacial area and surface tension respectively; and the subscripts L, S, and V indicate liquid, solid, and vapor, respectively. The first term on the right-hand side of equation (3) denotes the kinetic energy of the flowing liquid. The second, third, and fourth terms denote solid-liquid, solid-vapor, and liquid-vapor interfacial energies, respectively. The strategy is to compute the total system energy for each flow regime as a function of flow rate.

3.1. Conceptual Models

[17] The observations of *Schmuki and Laso* [1990] lead us to recognize at least three distinct flow regimes that are likely to occur in unsaturated fractures. These are, from the lowest-flow rate to the highest, sliding drop flow, rivulet flow, and falling film flow. These flow regimes are schematically illustrated in Figure 2 and briefly defined below.

[18] At very low-flow rate, sliding of fine drops is the dominant mechanism of flow. Sliding drops occur for example, when small quantity of liquid is sprayed on a solid surface (shower sprays on walls and rain drizzles on windshields). In this study, we assume the sliding drops in a train are equally spaced and that the trains are equally spaced as shown in Figure 2a.

[19] As the flow rate is increased, the sliding drops begin to touch forming slender threads or rivulets. Rivulet flow typically involves equidistant and identical threads of liquid with uniform cross section, as shown in Figure 2b. Rivulet flow is often observed on walls of shower rooms or automobile windshields, or as streaks of rain on concrete walls (see *Benson* [2001] for the latter example). In this study, we consider fully developed laminar rivulets, ignoring the detailed dynamics of finger formation at the boundaries of stable films.

[20] Falling film flow is defined as a complete wetting of the fracture surface by a sheet of liquid (Figure 2c). For the most part of this study, we consider laminar flow conditions with uniform film thickness that is directly proportional to the flow velocity. (Note that the (macroscopic) hydrodynamic film considered in this paper is much thicker and significantly different from "adsorbed" thin films whose thickness depends on chemical potential; see, e.g., *Or and Tuller* [2000] and *Tuller et al.* [1999] for the role of adsorbed films on flow and transport in porous media.) At very high flow rates these assumptions are invalid because such films are susceptible to waviness and instabilities arising from local surface tension differences and/or dominance of inertial forces. The waves usually travel at much faster velocities than the average film substrate and their description is expected to account for the episodicity that arises as a result of the fast waves [*Dragila*, 1999; *Dragila*

Table 2. Properties of Liquids Used by *Kim et al.* [2002] and Fitted Empirical Constants

	Liquid Properties			Fitted Constants		
Liquid	ρ, kg m^{-3}	μ, Pa s	σ_{LV}, N m^{-1}	θ_0, rad	γ	$\Delta\theta$
Ethylene glycol	1114	0.0209	0.0484	1.225	0.0015	0.0004
Glycerin (80 wt%) water (20 wt%)	1228	0.0600	0.0641	1.285	0.0020	0.0009
Glycerin	1260	0.95	0.063	1.363	0.0016	0.0006
Water[a]	998.2	0.00102	0.0727	$\pi/9$	0.003[b]	0.001[b]

[a]Water was not used in the experiments of *Kim et al.* [2002].
[b]These values were used for water on rock surface in the illustrative examples.

and Wheatcraft, 2001]. An upper limit to the stable film flow regime is provided in section 4.5 based on the Reynolds number.

[21] In sections 3.2–3.4, simplified geometries and flow equations of the flow regimes described above are introduced. A Cartesian coordinate system with the flow rate aligned parallel to the z axis is used, as shown in Figure 2. In all the cases, the system is assumed to be isothermal, and the wetting fluid is considered incompressible with constant Newtonian-viscosity μ and density ρ. A passive nonwetting fluid (e.g., air in an air-water system) is considered. Fluid flow is driven by the gravitational potential gradient,

$$\Xi = \rho g \cos(\alpha) \tag{4}$$

where α is the fracture inclination angle measured from the vertical. The liquid flow on the fracture surface is described by the equations of momentum conservation and continuity

$$\nabla^2 u - \beta = 0 \tag{5}$$

where u is the liquid velocity and $\beta = \Xi/\mu$. We consider a constant fracture flux given by,

$$q = Q/W \tag{6}$$

where Q is volumetric flow rate and W is the transverse fracture width.

3.2. Sliding Drops

[22] The importance of sliding drops to flow in unsaturated fractures was recently highlighted by *Doe* [2001]. The geometry of sliding drops involves a free surface whose configuration is nonlinearly dependent upon the volume and velocity. Because of this complexity, there are only a few studies that have attempted to describe the problem of sliding drops based on first principles. Recently, *Podgorski et al.* [2001] showed that small drops sliding down a slightly hydrophobic surface assume different shapes depending on their capillary number,

$$Ca = \mu v_d/\sigma_{LV} \tag{7}$$

where v_d is the velocity of the drop. Without going into a detailed description of the three-dimensional flow field and exact geometry of the associated free surface, *Podgorski et al.* [2001] derived a force balance based scaling law relating the drop volume to the sliding velocity that takes the following into consideration: (1) The drop velocity (v_d) is governed by the in-plane component of its weight $\rho g V_d \cos\alpha$, where V_d is the drop volume. (2) A typical viscous drag of order $\mu v_d V_d^{1/3}$ resists the sliding velocity. (3) A capillary force induced by of the nonuniformity of the contact angle along the perimeter of the drop resists the weight. This resistance scales as $\Delta\theta\sigma_{LV}V_d^{1/3}$, where $\Delta\theta$ is a perimeter-averaged projection factor of surface tension.

[23] The scaling law is written in terms of nondimensional numbers as

$$Ca = \gamma\, Bo \cos\alpha - \Delta\theta \tag{8}$$

where $Bo = V^{2/3}\rho g/\sigma_{LV}$ is the Bond number and γ is a proportionality constant. *Podgorski et al.* [2001] compared equation (8) with data from experiments using silicone-oil droplets on surfaces coated with fluoro-polymer. Their plots suggest that γ and $\Delta\theta$ are almost identical for the rounded and cornered drop shapes. However, the cusped drops have significantly higher γ and $\Delta\theta$ values. In the above scaling law γ and $\Delta\theta$ are empirical constants that depend on the fluid and solid properties. For subsequent analyses we estimate these constants from experimental data of *Kim et al.* [2002] who determined the sliding velocity of drops with known volume on smooth polycarbonate planes inclined at different angles. We plotted their data in terms of the dimensionless numbers (see Figure 4) and fitted equation (8) to the data. The properties of the liquids used in the experiments and the best fit γ and $\Delta\theta$ values are listed in Table 2. The data in Table 2 suggest that the fitted γ and $\Delta\theta$ are weakly related to viscosity, but both seem to increase with surface tension. Because the surface tension of glycerin is the closest to that of water, in subsequent illustrative calculations the values of γ and $\Delta\theta$ corresponding to glycerin are considered as representative of water on rock surface.

[24] Small drops, whose characteristic size (radius) is smaller than the capillary number, have spherical cap shape on a horizontal plane. For simplicity, we ignore the distortion from this ideal geometry and assume the drop shape is a spherical cap at all times as shown in Figure 3. The radius of the equivalent spherical drop is related to the drop volume by

$$R_d = V_d^{1/3}\left\{\frac{3}{4\pi\sin^4(\theta_0/2)(2+\cos\theta_0)}\right\}^{1/3} \tag{9}$$

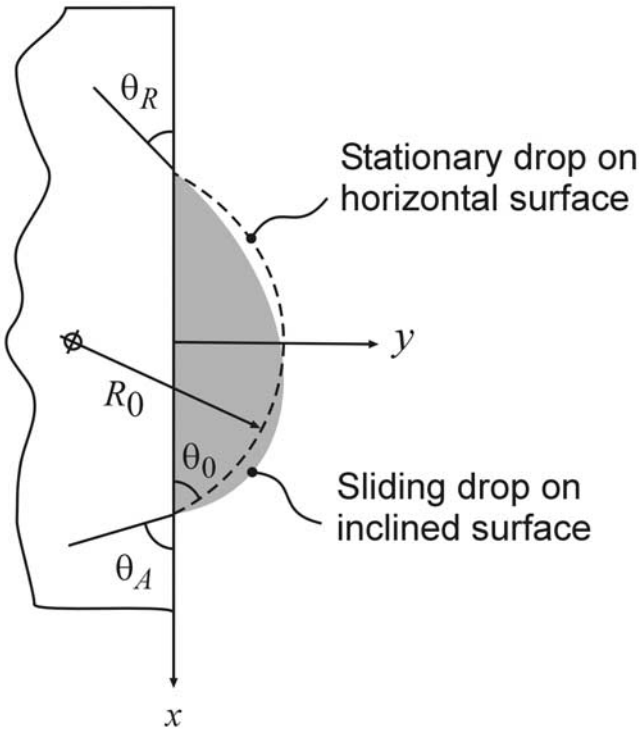

Figure 3. Definition of variables representing a sliding drop.

[25] The sliding velocity of the drop is related to the drop volume according to equation (8), which can be rearranged as

$$v_d = \gamma\beta V_d^{2/3} - \frac{\sigma_{LV}}{\mu}\Delta\theta \tag{10}$$

[26] Consider there are n_d drop paths per width W and that the number of drops in the train of drops in a fracture of length L is m_d, as illustrated in Figure 2a. The time it takes for an individual drop to traverse the axial interdrop separation distance $x_d = L/m_d$ is $t_d = x_d/v_d$. Then, flux equation (6) can be rewritten as

$$q = \frac{n_d}{W}\frac{V_d}{t_d} = \frac{n_d m_d}{L} V_d v_d \tag{11}$$

Upon substitution of equation (10) in equation (11) we arrive at

$$q = \frac{n_d}{W}\frac{m_d}{L} V_d\left(\gamma\beta V_d^{2/3} - \frac{\sigma_{LV}}{\mu}\Delta\theta\right) \tag{12}$$

Equation (12) cannot be solved for V_d in closed form.

[27] From the geometry shown in Figure 3 the liquid-vapor, soil-liquid, and solid-vapor interface areas are given, respectively, by

$$A_{LV} = n_d m_d 2\pi R_d^2(1 - \cos\theta_0) \tag{13}$$

$$A_{SL} = n_d m_d \pi R_d^2 \sin^2\theta_0 \tag{14}$$

$$A_{SV} = WL - A_{SL} = WL - n_d m_d \pi R^2 \sin^2\theta_0 \tag{15}$$

[28] Because the drops travel as unit masses the kinetic energy of individual sliding drop is simply $\rho V_d v_d^2/2$. The total energy (equation (3)) of the sliding drops is then,

$$E_d = \frac{n_d m_d \rho V_d v_d^2}{2} + A_{LV}\sigma_{LV} + A_{SL}\sigma_{SL} + A_{SV}\sigma_{SV} \tag{16}$$

Substituting equation (1) and equations (13)–(15) in equation (3) and simplifying it using equations (9) and (10) gives the relative sliding drops energy e_d as a function of the flux q, the number of drop trains (n_d/W), the number of sliding drops per train (m_d/L), and the equilibrium contact angle (θ_0)

$$\begin{aligned} e_d(q, n_d, m_d, \theta_0) &= \frac{E_d}{WL} - \sigma_{SL} \\ &= \frac{WL}{n_d m_d}\frac{\rho q}{2V_d} + \sigma_{LV}\left\{\frac{n_d m_d}{WL}\left(\frac{3}{4\pi}\right)^{2/3} V_d^{2/3} \right. \\ &\quad \left. \cdot \frac{\pi(2 - 2\cos\theta_0 + \sin^2\theta_0)}{\left[\sin^4(\theta_0/2)(2 + \cos\theta_0)\right]^{2/3}} + \cos\theta_0\right\} \end{aligned} \tag{17}$$

where the drop volume V_d is implicitly given as a function of the flux q by equation (12).

3.3. Rivulet Flow

[29] We employ two approximations regarding the rivulet geometry and the velocity profile to facilitate the derivation

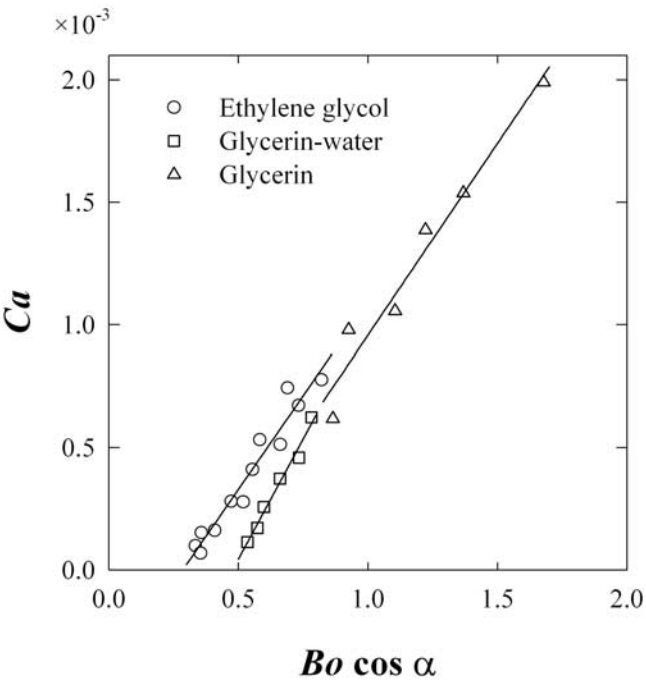

Figure 4. Relationship between capillary number and Bond number for sliding drops of different liquids on smooth polycarbonate surface [*Kim et al.*, 2002] and fitted scaling law given by equation (8) [*Podgorski et al.*, 2001].

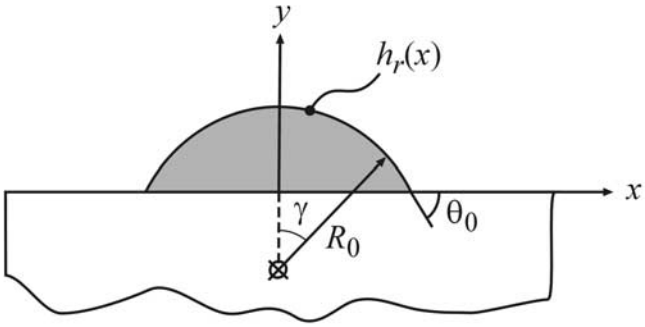

Figure 5. Schematic representation of the cross section of a straight rivulet.

of analytical expressions for the total system energy given later in this section. First, we assume that the capillary pressure is uniform throughout the cross section of the rivulet [*Mikielewicz and Moszynski*, 1976]. This assumption implies that the rivulet cross section can be represented by a circular arc of radius R_r, as illustrated in Figure 5 [*Bankoff*, 1971]. Then, the liquid-vapor interface is parametrically given by

$$h_r(x) = R_r(\cos\gamma - \cos\theta_0) \tag{18}$$

where h_r is the rivulet height at a distance x from the axis of the rivulet ($x = R_r \sin\gamma$) and the polar subtended angle is $0 \le \gamma \le \theta_0$.

[30] Second, we consider zero-order approximation of the fluid velocity such that an infinitesimal slice of the rivulet, with a width of dx, behaves as a uniform falling film (see section 3.4) [*Bankoff*, 1971; *Towell and Rothfeld*, 1966]. Assuming the flow is fully developed and laminar, the steady state solution to the flow equation (5) yields a velocity profile given by

$$u_r(x,y) = \beta \cdot \left(h_r(x)y - \frac{y^2}{2}\right) \tag{19}$$

[31] *Allen and Biggin* [1974] showed that the approximate solution (19) matches reasonably well with the finite element solution of equation (5) except in the neighborhood of the edges. As the contact angle approaches $\pi/2$, the zero-order approximation fails because the slope of the liquid-vapor interface grows rapidly near the edges.

[32] Considering that there are n_r identical rivulets across a fracture of width W, the total flow rate of all the rivulets is given by,

$$Q = n_r \int_{-w_r/2}^{w_r/2} \int_0^{h(x)} u_r(x,y)\mathrm{d}y\mathrm{d}x = \frac{2n_r}{3}\beta R^4 f_1(\theta_0) \tag{20}$$

where the rivulet width is

$$w_r = 2R_r \sin\theta_0 \tag{21}$$

and the function $f_1(\theta_0)$ is given by,

$$\begin{aligned} f_1(\theta_0) &= \int_0^{\theta_0} \cos\theta(\cos\theta - \cos\theta_0)^3 d\theta \\ &= \frac{36\theta_0 + 24\theta_0\cos 2\theta_0 - 28\sin 2\theta_0 - \sin 4\theta_0}{32} \end{aligned} \tag{22}$$

By rearranging equation (20) the rivulet radius can be expressed as a function of the flux as

$$R_r = \left(\frac{3q}{2(n_r/W)\beta f_1(\theta_0)}\right)^{1/4} \tag{23}$$

The fraction of the fracture width not wetted by the flowing rivulets is given as

$$\frac{d_r}{W} = 1 - \frac{n_r}{W}w_r = 1 - 2\frac{n_r}{W}R_r\sin\theta_0 \tag{24}$$

Strictly speaking, the dry space may be lined with very thin layer of adsorbed film [*Tuller et al.*, 1999]; nevertheless, its contribution compared to the rivulet flow is negligible.

[33] From equations (21) and (24) we note that the wetted and dry portions of the fracture surface area $L \times W$ are given by Ln_rw_r and LWd_r, respectively. The liquid-vapor interface area is $2Ln_rR_r\theta_0$. Then, for n_r straight rivulets with velocity profiles given by equation (19), the total energy equation (3) is rewritten as

$$\begin{aligned} E_r = &\int_{-w_r/2}^{w_r/2} \int_0^{h(x)} \frac{Ln_r\rho}{2} u_r(x,y)^2 \mathrm{d}y\mathrm{d}x \\ &+ L(n_rw_r\sigma_{SL} + Wd_r\sigma_{SV} + 2n_r\theta_0R_r\sigma_{LV}) \end{aligned} \tag{25}$$

Substituting equation (1) in equation (25) and rearranging gives the relative rivulet energy e_r as a function of the flux (q), the number of rivulets (n_r), and the equilibrium contact angle (θ_0):

$$\begin{aligned} e_r(q,n_r,\theta_0) = \frac{E_r}{WL} - \sigma_{SL} = &\frac{\rho\beta^2}{15}\frac{2n_r}{W}f_2(\theta_0)R_r^6 \\ &+ \sigma_{LV}\left\{\frac{2n_r}{W}R_r\left(\theta_0 - \frac{\sin 2\theta_0}{2}\right) + \cos\theta_0\right\} \end{aligned} \tag{26}$$

where R_r as a function of q is given by equation (23), and the function $f_3(\theta_0)$ is given by,

$$\begin{aligned} f_2(\theta_0) &= \int_0^{\theta_0} \cos\theta(\cos\theta - \cos\theta_0)^5 d\theta \\ &= \frac{1}{192}[600\theta_0 + 60\theta_0(10\cos 2\theta_0 + \cos 4\theta_0) \\ &\quad -425\sin 2\theta_0 - 101\sin 4\theta_0 - \sin 6\theta_0] \end{aligned} \tag{27}$$

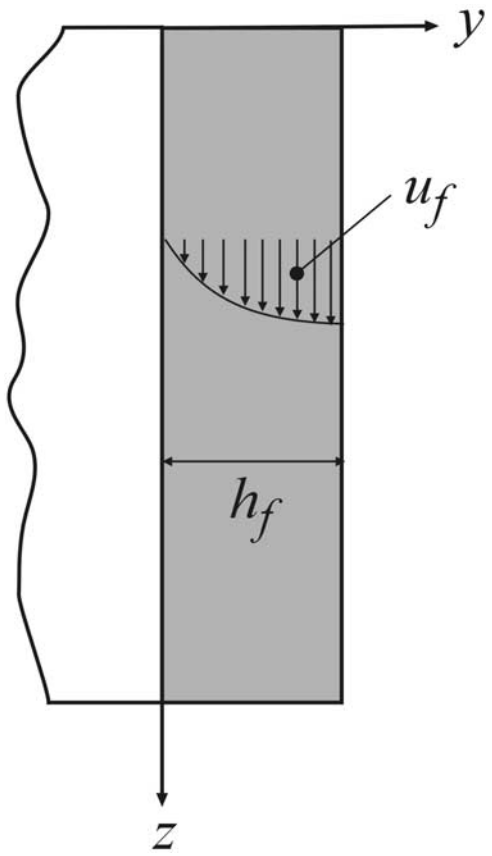

Figure 6. Schematic representation of a falling film and its velocity profile.

El-Genk and Saber [2001] provided a detailed review and verification of a slightly different form of equation (27).

3.4. Falling Film Flow

[34] The profile of a falling film (in the direction of flow) is assumed to be of uniform thickness, as shown in Figure 6. The thickness of such stable and flat films is commonly referred to as "Nusselt film thickness" [e.g., see *Dragila*, 1999, p. 48]. Assuming the flow is fully developed and laminar, the steady state solution to the flow equation (5) yields a velocity profile given by

$$u_f(y) = \beta\left(h_f y - \frac{y^2}{2}\right) \tag{28}$$

where h_f is the film thickness. The total volumetric flow rate is defined as the product of the average velocity (obtained by integrating the film velocity (equation (28)) along the film thickness) and film cross-sectional area ($h_f \times W$),

$$Q = Wh_f \int_0^{h_f} u_f \mathrm{d}y = W\beta\frac{h_f^3}{3} \tag{29}$$

By rearranging equation (29), the film thickness can be expressed as a function of the flux q

$$h_f = \left(\frac{3q}{\beta}\right)^{1/3} \tag{30}$$

[35] When the entire fracture surface is covered with a flowing film, there is no exposed solid-vapor interface. As stated above the film is considered perfectly flat; hence the solid-liquid and liquid-vapor areas are equal to the fracture area ($W \times L$). For a falling film with a velocity profile given by equation (28), the total energy equation (3) is rewritten as

$$E_f = \int_0^{h_f} WL\frac{\rho}{2}u_f(y)^2\mathrm{d}y + WL(\sigma_{SL} + \sigma_{LV}) \tag{31}$$

Substituting equation (1) in equation (31) and rearranging gives the relative film energy e_f as a function of film thickness h_f, which in turn depends on the flux q as given by equation (30):

$$e_f(q) = \frac{E_f}{WL} - \sigma_{SL} = \frac{\rho\beta^2}{15}h_f^5 + \sigma_{LV} \tag{32}$$

[36] Note that equations (26) and (32) are similar in form. The main difference is that there are families of curves that describe the different number of rivulets and/or different contact angles. In subsequent sections, the relative film energy is compared with those of rivulets and sliding drops to identify the most likely flow regime for a given flow condition.

4. Constraints on Flow Regimes

[37] In this section, we compare the relative energies of different flow regimes and designate the regime with lowest energy as the most likely one for the given flow conditions. As indicated by the relative energy equations, the total energy is the sum of the kinetic and interfacial energies. What determines the most likely (stable) flow regime at a given flow condition is the relative importance of these components.

[38] For all subsequent illustrative calculations, we consider a set of liquid properties and solid-liquid contact angles that reasonably approximate a natural fracture-water system. The properties are listed in Table 2.

4.1. Sliding Drop Regime

[39] The relative energy curves of sliding drops (equation (17)) traveling along a single train ($n_d = 1$) for $m_d = 1$, 2, 3, and 4 are plotted in Figure 7a. At the lowest-flux range, a single sliding drop (per unit fracture length) has the lowest relative energy and is thus the most likely flow mechanism. At a flux of approximately 0.002×10^{-6} m^3 s^{-1} m^{-1}, the energy curves of $m_d = 1$ and $m_d = 2$ intersect; beyond the intersection, the two-drop condition has lowest energy. This implies, given a fixed flow rate, that two drops with larger liquid-vapor surface area (hence more interfacial potential energy) travel at a much slower speed (hence lower kinetic energy) such that the total energy of the two-drop configuration is lower than that of the one-drop regime. Similar transitions from $m_d = 2$ to $m_d = 3$ and $m_d = 3$ and $m_d = 4$ are shown in Figure 7a. The transitions from m_d to $m_d + 1$ are illustrated in Figure 7b as a function of flux. The exact transition from m_d to $m_d + 1$

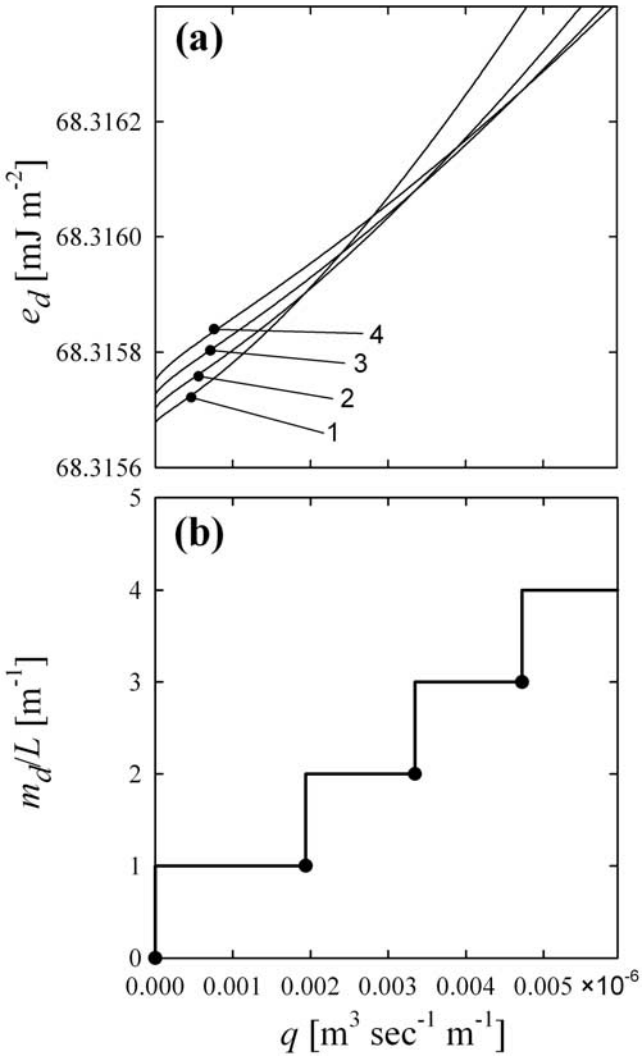

Figure 7. (a) Relative energy curves of sliding drops (e_d) as functions of flux (q) for 1, 2, 3, and 4 sliding drops and (b) the corresponding number of drops (m_d/L) satisfying the minimum energy configuration.

occurs when the respective relative energies (equation (17)) are identical, that is,

$$e_d(q_{dd}, n_d, m_d, \theta_0) = e_d(q_{dd}, n_d, m_d + 1, \theta_0) \tag{33}$$

where q_{dd} denotes the critical flux at which the transition from m_d to $m_d + 1$ occurs. Equation (33) was evaluated numerically and its values for the first few number of sliding droplets are shown in Figure 7b by circular symbols.

4.2. Transition From Sliding Drops to Straight Rivulet Flow Regime

[40] In Figure 8a the relative energy of sliding drops (equation (17)) for m_d/L = 1, 5, 10, 20, 50, 100 and 120 and the relative energy of one rivulet (n_r/W = 1) (equation (26)) are plotted over a wide range of flux (q). As the flow rate is increased, the number of drops sliding along a given train linearly increases; accordingly, the distance between the centers of two successive drops (L/m_d) decreases. When the drops begin to touch, a straight laminar rivulet is formed [*Schmuki and Laso*, 1990]. From the spherical cap approximation, this critical transition occurs when the drop diameter is equal to the interdrop distance. The critical flow rate at which the transition from drop regime to rivulet regime (q_{dr}) occurs is implicitly given by

$$\frac{L}{m_d} = 2R_d(q_{dr}) \sin\theta_0 \tag{34}$$

where R_d is the radius of the spherical cap drop as given by equation (23). In Figure 8b the number of drops as a function flow rate (given implicitly by equation (33)) and the transition from sliding drops to rivulet regime (given by the critical condition (34)) are plotted as a solid line and a solid dot, respectively.

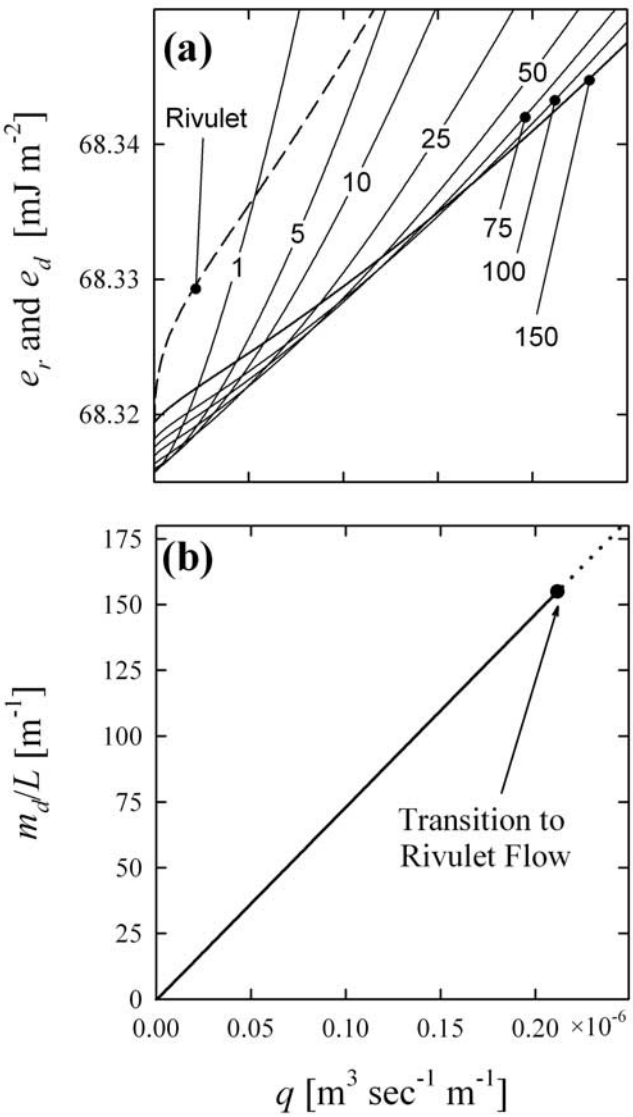

Figure 8. (a) Relative energy (e) curves as functions of flux (q) for several numbers of sliding drops along one train (m_d/L) and (b) the corresponding number of drops (m_d/L) satisfying the minimum energy configuration.

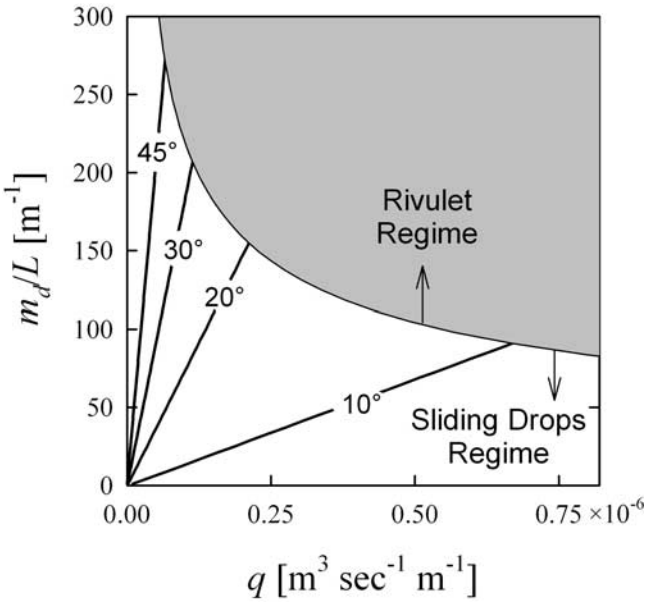

Figure 9. Number of sliding drops in one train (m_d/L) as a function of flux (q) for several contact angles (θ). The shaded region denotes rivulet flow regime.

[41] In Figure 9 we show the m_d to $m_d + 1$ transitions for a number of contact angles, as well as the envelope for droplet regime to rivulet regime transitions. At smaller contact angles, the drops are likely to leave a trail of thin film behind them [*Bico and Quere*, 2000] and the mechanism of transition from drop regime to rivulet regime described in this section is likely to overestimate the number of drops at this transition. This error is expected to be exacerbated by the fact that the flow rate at the transition is much smaller in small contact angles.

4.3. Rivulet Flow Regime

[42] We start by considering relative energies of a few rivulets e_r. In Figure 10a, relative energies (equation (26)) for one, two, three and four-rivulet scenarios (n_r/W = 1, 2, 3 and 4, respectively) are plotted as a function of flux q. At low flux, a single rivulet has the lowest energy and is thus the most likely flow mechanism. At a flux of approximately 0.25 × 10^{-6} m^3 s^{-1} m^{-1}, the energy curves of one-rivulet and two-rivulet scenarios intersect. When the flux‘ is increased beyond this critical value, the contribution of the kinetic energy gain to the single-rivulet system is more significant compared to the two-rivulet system, which has larger liquid-vapor interface area but smaller velocity. Hence the two-rivulet system becomes the more stable (preferable) configuration. Similar transitions to higher number of rivulets occur at higher-flow rates; the first few transitions are shown in Figure 10b. The exact transition from n_r to $n_r + 1$ occurs when the respective relative energies (equation (26)) are identical,

$$e_r(q_{rr}, n_r, \theta_0) = e_r(q_{rr}, n_r + 1, \theta_0) \tag{35}$$

where q_{rr} is the critical flux at which transition from n_r to $n_r + 1$ takes place. Solving equation (35) for q_{rr} and algebraic manipulation gives,

$$q_{rr}(n_r, \theta_0) = \left(\frac{2\beta}{3}\right)^{1/5} \frac{f_1(\theta_0)}{W} \left\{ \frac{5}{f_2(\theta_0)} \frac{\sigma_{LV}}{\rho\beta} (2\theta - \sin 2\theta) \cdot \sqrt{n_r(1+n_r)} \frac{(1+n_r)^{3/4} - n_r^{3/4}}{(1+n_r)^{1/2} - n_r^{1/2}} \right\}^{4/5} \tag{36}$$

Equation (36) is plotted in Figure 10b for n_r = 1, 2, and 3 as the circles. We further note that

$$\sqrt{n_r(1+n_r)} \frac{(1+n_r)^{3/4} - n_r^{3/4}}{(1+n_r)^{1/2} - n_r^{1/2}} \approx \frac{3}{2}\left(n_r + \frac{1}{2}\right)^{5/4} \tag{37}$$

The maximum error introduced by equation (37) is 7% for n_r = 1; it is less than 1% for $n_r > 3$ and less than 0.1% for

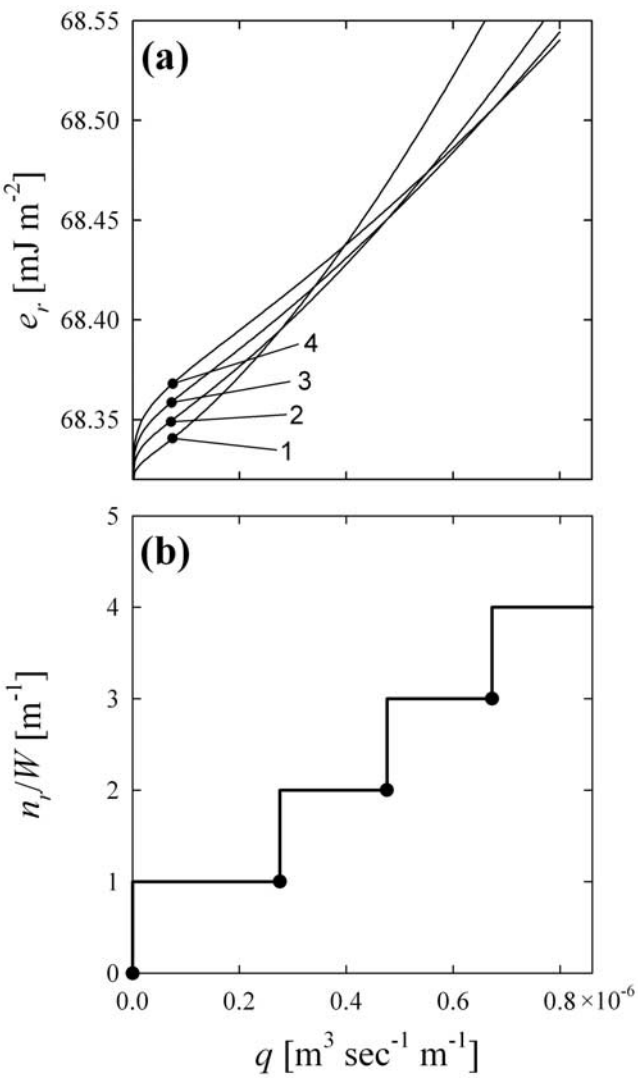

Figure 10. (a) Relative energy curves (e_r) as a function of flux (q) for 1, 2, 3 and 4 parallel rivulets and (b) the corresponding number of rivulets (n_r/W) satisfying the minimum energy configuration.

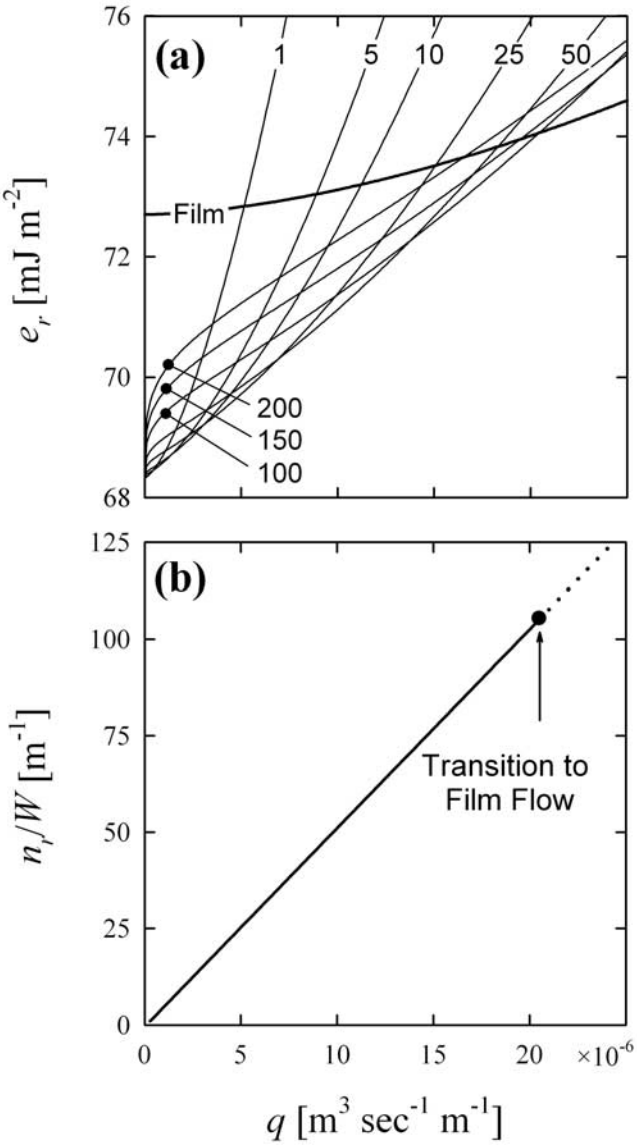

Figure 11. (a) Relative energy curves (e) as a function of flux (q) for several numbers of parallel rivulets (n_r/W) and a stable film and (b) the corresponding number of rivulets satisfying the minimum energy configuration.

$n_r > 11$. By substituting equation (37) in equation (36), and rearranging we obtain

$$\frac{n_{rr}}{W} = -1/2 + A_0 q_{rr} \tag{38}$$

where n_{rr} denotes the transition from n_r to $n_r + 1$, and the coefficient A_0 is

$$A_0 = (3/2)^{1/5}(2/15)^{4/5}\beta^{3/5}(\rho/\sigma_{LV})^{4/5}\left\{\frac{f_2(\theta_0)}{(2\theta - \sin 2\theta)f_1(\theta_0)^{5/4}}\right\}^{4/5} \tag{39}$$

Equation (38) indicates that the optimal number of rivulets n_{rr} is linearly related to the flux Q_{rr}. Furthermore, the slope of the relationship is a function of the contact angle θ_0 and the liquid properties.

4.4. Transition From Rivulet Flow Regime to Film Flow Regime

[43] In Figure 11a the relative energy of straights rivulets (equation (26)) for n_r/W = 1, 5, 10, 50, 100, 150 and 200, and the relative energy of stable film (equation (32)) are plotted over a wider range of flux (q). The n_r to $n_r + 1$ transitions (equation (36)) are plotted as a function of the critical flow rate q_{rr} in Figure 11b. Notice in Figure 11a that the rivulet energy curves, up to approximately $n_r/W = 100$, cross the film energy curve at progressively increasing flow rates. Moreover, notice that within this flow rate range, all the transitions from n_r to $n_r + 1$ occur while the rivulet energies are below that of the film; therefore the stable flow regime is rivulet flow. Beyond this critical flow rate, all the n_r to $n_r + 1$ transitions occur while the rivulet energies are higher than the film energy. In the following, we derive expressions for the critical flow rate at which a stable film breaks apart into multiple rivulets, and calculate the corresponding maximum number of rivulets. First, the flow rate at which the rivulet energy curve with an arbitrary n_r intersects the film energy curve, $e_r(q, n_r, \theta_0) = e_f(q)$, is obtained by equating (26) and (32) and factoring out q and n_r/W:

$$A_1 q^{5/3} + A_2\left(\frac{n_r}{W}\right)^{-1/2} q^{3/2} + A_3\left(\frac{n_r}{W}\right)^{3/4} q^{1/4} + A_4 = 0 \tag{40}$$

where

$$A_1 = -\frac{3^{2/3}}{5}\beta^2\rho\beta^{-5/3}$$

$$A_2 = \frac{\sqrt{3/2}}{5}\beta^2\rho f_2(\theta_0)\cdot(f_1(\theta_0)\beta)^{-3/2}$$

$$A_3 = 2^{3/4}3^{1/4}\sigma_{LV}\left(\theta_0 - \frac{\sin 2\theta_0}{2}\right)(f_1(\theta_0)\beta)^{-1/4}$$

$$A_4 = \sigma_{LV}(1 - \cos\theta_0)$$

[44] The condition for the transition from rivulet flow regime to film flow regime requires finding the largest n_r to $n_r + 1$ transition that satisfies $e_r(q, n_r, \theta_0) \le e_f(q)$. Thus a substituting equation (38) in equation (40) we obtain

$$A_1 q_{rf}^{5/3} + A_2\left(A_0 q_{rf} - 1/2\right)^{-1/2} Q_{rf}^{3/2} + A_3\left(A_0 q_{rf} - 1/2\right)^{3/4} q_{rf}^{1/4} + A_4 = 0 \tag{41}$$

where q_{rf} stands for the critical flux at the transition from film flow to rivulet flow regime (or vise versa). Note that equation (41) has to be evaluated numerically to obtain q_{rf} as a function of the fluid properties and contact angle. In Figure 11b, q_{rf} was calculated for the standard liquid and contact angle using equation (41) and the respective n_{rf} was obtained from equation (38). This transition point from rivulet flow to film flow is designated by a black dot. To highlight the importance of contact angle in the break up of film to rivulets and the transitions within the rivulet flow regime the n_r to $n_r + 1$ transitions (equation (38)) are plotted in Figure 12 for a number of contact angles. An envelope

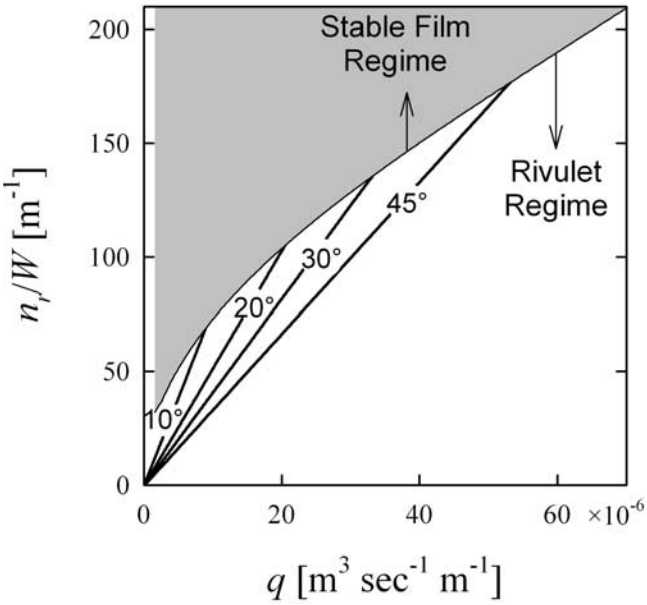

Figure 12. Number of rivulets (n_r/W) as a function of flux (q) for several contact angles. The shaded region denotes film flow.

marking the transition from rivulet regime to film regime is also shown (equations (41) and (38)). The two important results of this plot are (1) the critical flow rate at which a stable film breaks up to rivulets increases with increasing contact angle, and (2) the maximum number of rivulets at this breakdown increases with increaseing contact angle.

4.5. Instability of the Film Flow Regime

[45] The Nusselt's film flow equation assumes that the film surface is free of any ripples and waves. This assumption works only under low to intermediate Reynolds number. *Patnaik and Perez-Blanco* [1996] provided classification of the film flow regime based on stability. Their classification depends on the Reynolds number:

$$Re_S \equiv 4Re = \frac{4q\rho}{\mu} \tag{42}$$

[46] The Nusselt's film flow typically occurs in the $Re_S \leq 20$ range. Films with high-frequency low-amplitude capillary waves occur in the range $20 < Re_S < 200$. These capillary waves originate when variations in surface tension caused by localized temperature and concentration gradients are comparable to the gravity and viscous forces. However, "statistical analysis shows that the mean film thickness for wavy film is close to the stable state value for flat films when the film is thin (i.e., low Reynolds numbers)" [*Dragila*, 1999]. Thus we regard the Nusselt's approximation to hold for $Re_S \leq 200$.

[47] For $Re_S > 200$, the main cause of the perturbation is an inertial force. The resulting waves can be laminar ($200 < Re_S < 1000$) or turbulent ($1000 < Re_S < 4000$). These waves roll over the substrate film at a much higher velocity than the substrate. The flat film surface solutions no longer apply in this range. When $Re_S > 4000$, the flow is fully turbulent. The unstable flows at very high flow rates (on the order of $Re_S \geq 1000$) are considered to be beyond the interest of hydrological applications.

5. Summary and Conclusions

[48] Using simplified flow geometries and assuming laminar flow, we derived energy equations for the major flow regimes that are likely to occur in fractured systems. The energy equations were used to provide constraints on the flow rates that allowed us to delineate the flow regimes. The potential implications of the results presented in this paper become apparent when looking at all the transitions over wide ranges of flow rate and wettability of the fracture surface. The transitions from drop sliding regime to rivulet regime, from rivulet regime to stable film regime, and onset of waviness and turbulence on films are shown by plotting equations (34) and (41) and instability conditions specified in section 4.5 (see Figure 13). The flow rate spectrum in Figure 13 covers several orders of magnitude, and the contact angles range from slightly hydrophobic ($\theta_0 \approx 0°$) to moderately hydrophobic ($\theta_0 \approx 90°$). These results depict the boundaries between flow regimes for a vertical fracture. According to Figure 13, steady flow (stable film and rivulets) occurs only in the intermediate flow rate range. Outside of this region, a steady and constant input flux yields an episodic flow downstream. At lower-flow rates, episodicity emanates from disintegration of rivulets into trains of sliding drops. At higher-flow rates, destabilization of films by surface waves is responsible for episodic flows.

[49] As shown in Figure 13, an elevated contact angle (reduced wettability) broadens the range of the steady flow regimes. At high contact angles, the weak adhesion of liquids onto the fracture surfaces decreases the tendency for rivulets to breakup into drops, as shown by the rapid decrease of the flux at which transition from sliding drops to rivulet regime occurs.

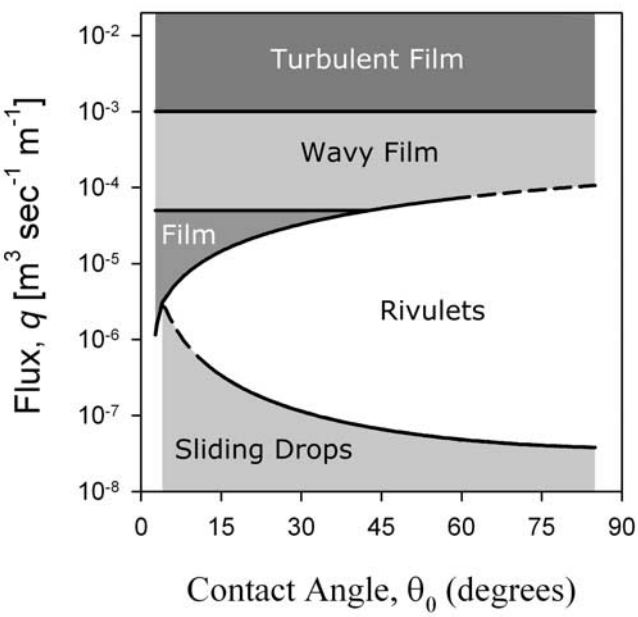

Figure 13. Summary of dominant flow regimes for wide ranges of contact angle (θ) and flux (q).

[50] The flux at which transition from rivulet regime to stable film flow occurs increases with contact angle. This is because the ratio of the rivulet cross-sectional area to its liquid-vapor interface area decreases with contact angle (see Figure 5), allowing the rivulets to transport liquid at higher-flow rates but lower potential energy compared to films. At a contact angle of $\theta_0 \approx 45°$, the possibility for stable films to form on vertical fractures is eliminated. Note that for fracture inclination angles other than vertical, the curves in Figure 13 are expected shift; nevertheless, the general trend remains the same.

[51] The main conclusions drawn from this study are as follows: (1) Even for idealized smooth fracture surfaces, slight variations in contact angle and/or fracture inclination angle can result in dissimilar flow regimes under a given flow rate. (2) Dissimilar flow regimes can coexist in a fractured rock, if the rock comprises fracture surfaces with different inclination angles and/or wettability. Thus a realistic self-consistent flow model should be able to discern and apply the appropriate conceptual model fitting for any given flow condition. (3) The implications of assuming a wrong flow regime are far-reaching. For example, the fracture-matrix interaction is less significant in a rivulet regime compared to films. In addition, particles in rivulets travel at much slower velocity than in films (under identical volumetric flux per cross section). The consequences of these differences to solute diffusion and/or travel time are apparent.

[52] The results of this study can be directly applied to flow visualization experiments and conceptual models of unsaturated flow in fractures that utilize ''smooth fracture surfaces''. Moreover, it should also be noted that the results are admissible for fractures with very fine roughness; if the effect of the roughness can be described using contact angle as discussed in section 2.2. Extension of the proposed constraints to macroscopically rough fractures and/or fracture networks requires further experimental and theoretical studies.

[53] **Acknowledgments.** This work was supported by the Director, Office of Science, of the U.S. Department of Energy under contract DE-AC03-76SF00098, through the Ernest Orlando Lawrence Berkeley National Laboratory (LBNL), Earth Sciences Division. Thorough reviews by Stefan Finsterle, Grace Su, two anonymous reviewers, and an associate editor of WRR helped improve the quality of the manuscript.

References

Adamson, A. W., and A. P. Gast (1997), *Physical Chemistry of Surfaces*, John Wiley, Hoboken, N. J.

Allen, R. F., and C. M. Biggin (1974), Longitudinal flow of a lenticular liquid filament down an inclined plane, *Phys. Fluids*, *17*(2), 287–291.

Amundsen, H., G. Wagner, U. Oxaal, P. Meakin, J. Feder, and T. Jossang (1999), Slow two-phase flow in artificial fractures: Experiments and simulations, *Water Resour. Res.*, *35*(9), 2619–2626.

Bankoff, S. G. (1971), Minimum thickness of a draining liquid film, *Int. J. Heat Mass Transfer*, *14*(12), 2143–2146.

Bankoff, S. G. (1983), Problems in interfacial instability, *Ann. N. Y. Acad. Sci.*, *404*, 405–419.

Benson, D. A. (2001), A model of water streaking down a wall, *Water Resour. Res.*, *37*(2), 427–430.

Berbente, C. P., and E. Ruckenst (1968), Hydrodynamics of wave flow, *AIChE J.*, *14*(5), 772–782.

Berkowitz, B. (2002), Characterizing flow and transport in fractured geological media: A review, *Adv. Water Resour.*, *25*(8–12), 861–884.

Bertels, S. P., D. A. DiCarlo, and M. J. Blunt (2001), Measurement of aperture distribution, capillary pressure, relative permeability, and in situ saturation in a rock fracture using computed tomography scanning, *Water Resour. Res.*, *37*(3), 649–662.

Bico, J., and D. Quere (2000), Liquid trains in a tube, *Europhys. Lett.*, *51*(5), 546–550.

Brauner, N. (1989), Modelling of wavy flow in turbulent free falling films, *Int. J. Multiphase Flow*, *15*(4), 505–520.

Cassie, A. B. D. (1948), Contact angles, *Discuss. Faraday Soc.*, *3*, 11–16.

Dettre, R. H., and R. E. Johnson (1964), Contact angle hysteresis. II. Contact angle measurements on rough surfaces, *Adv. Chem. Ser.*, *43*, 136–144.

Detwiler, R. L., H. Rajaram, and R. J. Glass (2002), Experimental and simulated solute transport in a partially-saturated, variable-aperture fracture, *Geophys. Res. Lett.*, *29*(8), 1272, doi:10.1029/2001GL013508.

Dobson, P. F., T. J. Kneafsey, J. Hulen, and A. Simmons (2003), Porosity, permeability, and fluid flow in the Yellowstone geothermal system, Wyoming, *J. Volcanol. Geotherm. Res.*, *123*(3–4), 313–324.

Doe, T. W. (2001), What do drops do? Surface wetting and network geometry effects on vadose-zone fracture flow, in *Conceptual Models of Flow and Transport in the Fractured Vadose Zone*, pp. 243–270, Natl. Acad. Press, Washington, D. C.

Dragila, M. I. (1999), A new theory for transport in unsaturated fractures: Free-surface film flows, Ph.D. thesis, Univ. of Nev., Reno.

Dragila, M. I., and N. Weisbrod (2003), Parameters affecting maximum fluid transport in large aperture fractures, *Adv. Water Resour.*, *26*, 1219–1228.

Dragila, M. I., and S. W. Wheatcraft (2001), Free-surface films, in *Conceptual Models of Flow and Transport in the Fractured Vadose Zone*, pp. 217–242, Natl. Acad. Press, Washington, D. C.

El-Genk, M. S., and H. H. Saber (2001), Minimum thickness of a flowing down liquid film on a vertical surface, *Int. J. Heat Mass Transfer*, *44*(15), 2809–2825.

Fourar, M., S. Bories, R. Lenormand, and P. Persoff (1993), Two-phase flow in smooth and rough fractures: Measurement and correlation by porous-medium and pipe flow models, *Water Resour. Res.*, *29*(11), 3699–3708.

Glass, R. J., and M. J. Nicholl (1996), Physics of gravity fingering of immiscible fluids within porous media—An overview of current understanding and selected complicating factors, *Geoderma*, *70*(2–4), 133–163.

Glass, R. J., M. J. Nicholl, A. L. Ramirez, and W. D. Daily (2002), Liquid phase structure within an unsaturated fracture network beneath a surface infiltration event: Field experiment, *Water Resour. Res.*, *38*(10), 1199, doi:10.1029/2000WR000167.

Hakami, E., and E. Larsson (1996), Aperture measurements and flow experiments on a single natural fracture, *Int. J. Rock Mech. Min. Sci. Geomech. Abst.*, *33*(4), 395–404.

Hobler, T. (1964), Minimum surface wetting (in Polish), *Chem. Stosow., Ser. B*, *2*, 145–159.

Hughes, D. T., and T. R. Bott (1998), Minimum thickness of a liquid film flowing down a vertical tube, *Int. J. Heat Mass Transfer*, *41*(2), 253–260.

Jayanti, S., and G. F. Hewitt (1997), Hydrodynamics and heat transfer of wavy thin film flow, *Int. J. Heat Mass Transfer*, *40*(1), 179–190.

Joo, S. W., S. H. Davis, and S. G. Bankoff (1996), A mechanism for rivulet formation in heated falling films, *J. Fluid Mech.*, *321*, 279–298.

Kim, H.-Y., H. J. Lee, and B. H. Kang (2002), Sliding of liquid drops down an inclined solid surface, *J. Colloid Interface Sci.*, *247*(2), 372–380.

Kneafsey, T. J., and K. Pruess (1998), Laboratory experiments on heat-driven two-phase flows in natural and artificial rock fractures, *Water Resour. Res.*, *34*(12), 3349–3367.

Lee, J. (1969), Kapitzas method of film flow description, *Chem. Eng. Sci.*, *24*(8), 1309–1319.

Mikielewicz, J., and J. R. Moszynski (1976), Minimum thickness of a liquid-film flowing vertically down a solid-surface, *Int. J. Heat Mass Transfer*, *19*(7), 771–776.

Muller, B., M. Riedel, R. Michel, S. M. De Paul, R. Hofer, D. Heger, and D. Grutzmacher (2001), Impact of nanometer-scale roughness on contact-angle hysteresis and globulin adsorption, *J. Vac. Sci. Technol. B*, *19*(5), 1715–1720.

National Academy of Sciences (1996), *Rock Fractures And fluid Flow: Contemporary Understanding and Applications*, Natl. Acad. Press, Washington, D. C.

Nicholl, M. J., R. J. Glass, and S. W. Wheatcraft (1994), Gravity-driven infiltration instability in initially dry nonhorizontal fractures, *Water Resour. Res.*, *30*(9), 2533–2546.

Or, D., and M. Tuller (2000), Flow in unsaturated fractured porous media: Hydraulic conductivity of rough surfaces, *Water Resour. Res.*, *36*(5), 1165–1177.

Packham, D. E. (2003), Surface energy, surface topography and adhesion, *Int. J. Adhesion Adhesives*, *23*(6), 437–448.

Patnaik, V., and H. Perez-Blanco (1996), Roll waves in falling films: An approximate treatment of the velocity field, *Int. J. Heat Fluid Flow*, *17*(1), 63–70.

Penev, V., C. Boyadjie, V. P. Vorotili, and V. S. Krylov (1972), Wavy flow of thin liquid films, *Int. J. Heat Mass Transfer*, *15*(7), 1395–1406.

Persoff, P., and K. Pruess (1995), Two-phase flow visualization and relative permeability measurement in natural rough-walled rock fractures, *Water Resour. Res.*, *31*(5), 1175–1186.

Podgorski, T., J. M. Flesselles, and L. Limat (2001), Corners, cusps, and pearls in running drops, *Phys. Rev. Lett.*, *87*(3), 036102, doi:10.1103/PhysRevLett.87.036102.

Ponter, A. B., and K. M. Aswald (1977), Minimum thickness of a liquid-film flowing down a vertical surface—Validity of mikielewicz and moszynskis equation, *Int. J. Heat Mass Transfer*, *20*(5), 575–576.

Pruess, K. (1999), A mechanistic model for water seepage through thick unsaturated zones in fractured rocks of low matrix permeability, *Water Resour. Res.*, *35*(4), 1039–1051.

Schmuki, P., and M. Laso (1990), On the stability of rivulet flow, *J. Fluid Mech.*, *215*, 125–143.

Soo, S. L. (1996), Instability in a falling liquid film, *Int. J. Heat Fluid Flow*, *17*(5), 526–527.

Su, G. W., J. T. Geller, K. Pruess, and F. Wen (1999), Experimental studies of water seepage and intermittent flow in unsaturated, rough-walled fractures, *Water Resour. Res.*, *35*(4), 1019–1037.

Su, G. W., J. T. Geller, K. Pruess, and J. R. Hunt (2001), Solute transport along preferential flow paths in unsaturated fractures, *Water Resour. Res.*, *37*(10), 2481–2491.

Summer, A. L., E. J. Menke, Y. Dubowski, J. T. Newberg, R. M. Penner, J. C. Hemminger, L. M. Wingen, T. Brauers, and B. J. Finlayson-Pitts (2004), The nature of water on surfaces of laboratory systems and implications for heterogeneous chemistry in the troposphere, *Phys. Chem. Chem. Phys.*, *6*(3), 604–613.

Tokunaga, T. K., and J. M. Wan (1997), Water film flow along fracture surfaces of porous rock, *Water Resour. Res.*, *33*(6), 1287–1295.

Tokunaga, T. K., and J. M. Wan (2001), Surface-zone flow along unsaturated rock fractures, *Water Resour. Res.*, *37*(2), 287–296.

Tokunaga, T. K., J. M. Wan, and S. R. Sutton (2000), Transient film flow on rough fracture surfaces, *Water Resour. Res.*, *36*(7), 1737–1746.

Towell, G. D., and L. B. Rothfeld (1966), Hydrodynamics of rivulet flow, *AiCHE J.*, *12*(5), 972–980.

Tuller, M., D. Or, and L. M. Dudley (1999), Adsorption and capillary condensation in porous media: Liquid retention and interfacial configurations in angular pores, *Water Resour. Res.*, *35*(7), 1949–1964.

Yih, C. S. (1963), Stability of liquid flow down an inclined plane, *Phys. Fluids*, *6*(3), 321–334.

Zhong, L. R., A. Mayer, and R. J. Glass (2001), Visualization of surfactant-enhanced nonaqueous phase liquid mobilization and solubilization in a two-dimensional micromodel, *Water Resour. Res.*, *37*(3), 523–537.

T. A. Ghezzehei, Earth Sciences Division, Lawrence Berkeley National Laboratory, MS 90R1116, 1 Cyclotron Road, Berkeley, CA 94720-8126, USA. (taghezzehei@lbl.gov)